TECHNISCHE MECHANIK
European Journal of Engineering Mechanics
Diamond Open Access
journal homepage: www.ovgu.de/techmech

Tech. Mech., Vol. 46, Is. 1, (2026), 55–65
Received: 27.10.2025
Accepted: 08.01.2026
Available online: 16.02.2026

Quantitative analysis of surface mode oscillations of acoustically excited microbubbles

Dániel Nagy[1]*, Péter Kalmár[1], Kálmán Klapcsik[1], and Ferenc Hegedűs[1]

[1] Department of Hydrodynamic Systems, Faculty of Mechanical Engineering, Budapest University of Technology and Economics. Műegyetem rkp. 3, H-1111 Budapest, Hungary

Abstract: This study investigates the non-spherical dynamics in acoustically driven microbubbles using two modeling approaches: a Reduced-Order Model (ROM) and Direct Numerical Simulations (DNS) performed with the ALPACA multiphase flow solver. The ROM couples the radial dynamics, described by the Keller–Miksis equation, with axisymmetric surface-mode oscillations, resulting in a computationally efficient framework for describing the non-spherical oscillations of bubbles. The DNS approach directly solves the governing compressible Navier–Stokes equations with interface-capturing making this approach computationally more expensive. Accurate interface-capturing and capillary calculations are critical for surface-mode oscillation in the DNS; thus, two different models are evaluated in this study: a sharp level set method and a diffuse-interface method. The diffuse-interface method demonstrates excellent agreement with the ROM in predicting both the spherical oscillations and stable surface-mode amplitudes, while the level set method tends to overdamp surface perturbations and is thus considered inaccurate for most cases involving non-spherical bubbles. Both the ROM and diffuse-interface–based DNS predict spherical stability and bubble breakup similarly, with bubble breakup occurring when surface-mode amplitudes diverge. These findings show that the ROM can serve as an efficient predictor of bubble breakup, while DNS simulations with the diffuse-interface approach provide detailed insight into the nonlinear dynamics and breakup processes. Together, these methods offer a robust and complementary framework for analyzing non-spherical bubble dynamics in acoustic fields.

Keywords: bubble dynamics, direct numerical simulation, multiphase flow, diffuse-interface, level set, reduced-order model

1 Introduction

The behavior of oscillating bubbles in acoustic fields forms a fundamental aspect of sonochemistry, where such bubbles serve as localized sites of intense energy concentration, driving chemical reactions Sochard et al. (1997); Kubicsek et al. (2024); Cho and Yun (2020); Al-Awamleh and Hegedűs (2024); Kubicsek et al. (2025); Hou et al. (2025); Wong et al. (2025). Under acoustic excitation, microbubbles exhibit a wide range of dynamic responses, including spherical oscillations Kameda and Matsumoto (1999); Prosperetti and Hao (1999); Ma et al. (2022), stable surface mode oscillations Cleve et al. (2019); Nagy et al. (2025); Wu et al. (2025), jet formation Rosselló et al. (2018); Prabowo and Ohl (2011); Nagy and Hegedűs (2025); Mnich et al. (2024); Denner et al. (2020), and even breakup Versluis et al. (2010); Mur et al. (2024). A detailed understanding of these phenomena is essential for the effective scaling of cavitation-based chemical synthesis toward industrial applications.

Modeling non-spherical bubble oscillations remains challenging due to uncertainties in both experimental and numerical approaches. Experimental data are available only for limited parameter ranges Versluis et al. (2010); Guédra and Inserra (2018); Cleve et al. (2019), and often suffer from measurement uncertainties. In particular, two-dimensional imaging cannot unambiguously reconstruct three-dimensional bubble shapes, as different axisymmetric modes may produce identical projections, and internal features – such as the case for jet formation – remain invisible Jia and Soyama (2024). On the computational side, reduced models rely on simplifying assumptions that may not capture nonlinear interactions accurately.

To address these challenges, this study combines two complementary modeling frameworks: a reduced-order model (ROM) and high-fidelity direct numerical simulations (DNS) using the ALPACA solver. The ROM, developed by Shaw (2006, 2009, 2017), provides an efficient tool for predicting coupled radial and surface-mode dynamics. It has been successfully applied for large-scale parametric studies and was even validated for certain cases with measurements by Kalmár et al. (2023, 2024). However, it is inherently limited to small surface perturbations. In contrast, ALPACA Hoppe et al. (2022a,b) is a fully compressible multiphase CFD solver capable of resolving nonlinear effects, including large-amplitude oscillations and bubble breakup, through an adaptive multiresolution mesh Nagy and Hegedűs (2023). In these DNS simulations, the accurate treatment of the liquid–gas interface is crucial for predicting surface-mode oscillations, as capillary forces dominate the dynamics near the bubble surface. Therefore, two interface-capturing schemes are tested within ALPACA: a sharp level set method by Osher and Fedkiw (2001), which supposedly provides high geometric fidelity but is prone to slight mass loss, and a diffuse-interface method introduced by Paula et al. (2023), which conserves mass and momentum precisely but represents the interface over a finite thickness.

The main objective of this work is to quantitatively assess the performance and consistency of these approaches in predicting the surface mode oscillations of acoustically excited microbubbles. Section 2 introduces the modeling framework and numerical

* E-mail address: dnagy@hds.bme.hu
doi: 10.24352/UB.OVGU-2026-007

schemes. Section 3 presents the convergence analysis and compares the DNS and ROM predictions across different excitation amplitudes for a selected case. Finally, the findings are discussed in Section 4, and the main conclusions are summarized in Section 5.

2 Methods

2.1 Reduced-Order Model

The Reduced-Order Model (ROM) handles the non-spherical bubble dynamics as a vibration problem assuming axial symmetry and small deformation. The aim is to avoid partial differential equations by employing modal decomposition, specifically using Legendre polynomials as orthogonal basis functions, and to construct an ordinary differential equation system that describes the time evolution of the mode amplitudes. In this manner, the temporal evolution of the complex bubble shape r_s, expressed via Legendre polynomials as an infinite series in a spherical coordinate system, can be described as:

$$r_s(\theta, t) = R(t) + \sum_{n=2}^{\infty} \varepsilon a_n(t) P_n(\mu), \tag{1}$$

where $R(t)$ is the spherical or 0^{th} mode as the function of time, while a_n denotes the n^{th} mode amplitude corresponding to the Legendre polynomial $P_n(\mu)$ of order n, with $\mu = \cos(\mu)$. Note that the first mode, i.e., the translational motion, is neglected in this paper for simplicity. Additionally, surface distortion is assumed to be small, as indicated by the small parameter ε. Following the work of Shaw (2006, 2009, 2017), the mode amplitudes are described by an implicit second-order nonlinear n-dimensional differential equation system derived from the Lagrangian function composed of the kinetic and potential energy. The nonlinear coupling terms permit interaction between the modes and account for the implicit nature of the system. The volume mode — corresponding to the radial oscillation $R(t)$ — reads as:

$$\left(1 - \frac{\dot{R}}{c_L}\right) R\ddot{R} + \left(1 - \frac{\dot{R}}{3c_L}\right) \frac{3}{2}\dot{R}^2 = G(t) + \frac{1}{c_L}\left(\dot{R} \cdot G(t) + R \cdot \dot{G}(t)\right) + \varepsilon^2 \left(g_0 + g_{0v}\right), \tag{2}$$

where c_L is the speed of sound in the liquid and

$$G(t) = \frac{p_{B_0}}{\rho_L}\left(\frac{R_0}{R}\right)^{3\gamma} + \frac{p_v}{\rho_L} - \frac{1}{\rho_L}\left(p_0 + p_A \sin(\omega t)\right) - \frac{4\mu_L \dot{R}}{\rho_L R} - \frac{2\sigma}{\rho_L R}. \tag{3}$$

In this context, p_{B_0} denotes the equilibrium pressure inside the bubble, while ρ_L represents the density of the liquid. The initial radius of the bubble is given by R_0, and γ refers to the ratio of specific heats. The dynamic viscosity of the liquid is denoted by μ_L, and σ stands for the surface tension. Acoustic excitation is characterized by the angular frequency $\omega = 2\pi f$ (where f is the frequency) and the pressure amplitude p_A. The ambient pressure, also known as the far-field pressure, is represented by p_0, and p_v indicates the vapour pressure. The higher order terms g_n and g_{nv} are the inviscid and damping terms, which can be found in Shaw (2006, 2009). The surface modes have the following form:

$$\varepsilon\Bigg\{R\ddot{a}_n + 3\dot{R}\dot{a}_n + \left[\left(n^2-1\right)(n+2)\frac{\sigma}{\rho_L R^2} - (n-1)\ddot{R}\right] a_n + \frac{2\mu_L}{\rho_L}\left[(n-1)(n+2)\frac{\dot{R}}{R^2}a_n + (n+2)(2n+1)\frac{\dot{a}_n}{R}\right]\Bigg\} = \varepsilon^2\left(g_n + g_{nv}\right). \tag{4}$$

Like the 0^{th} mode, the second-order term governs the coupling between the modes, which can be separated into inviscid and damping components; the interested reader can find these terms in Kalmár et al. (2023).
The solution strategy for the model is divided into two main parts: an initial value problem and a nonlinear equation system. The initial value problem is solved using an in-house Runge–Kutta–Cash–Karp solver. At the same time, the nonlinear equation system is handled using a GPU-optimized iterative technique derived in Kalmár et al. (2023). With this approach, the parameters of spherical or closely spherically oscillating bubbles can be found efficiently. The approximated validity limit of the model, i.e., the maximum of the relative mode amplitude (a_n/R) corresponding to the dominant mode (mode with the largest amplitude), is between 0.25 and 0.37 as estimated by Kalmár et al. (2024).

2.2 DNS Simulations

Direct numerical simulation (DNS) of an oscillating microbubble in an acoustic field requires a compressible multiphase flow solver capable of accurately resolving the coupled dynamics of the liquid and gas phases. The computational domain must typically span at least one acoustic wavelength to capture the standing wave field, which, based on the speed of sound and the excitation frequency, corresponds to a characteristic length of approximately 10 mm. In contrast, bubble diameters in sonochemical applications are on the order of 10 µm, resulting in a scale separation of roughly three orders of magnitude. This disparity imposes strict requirements on the numerical mesh, particularly in the vicinity of the bubble interface where oscillations occur. To accurately capture these localized dynamics, a highly refined grid resolution is essential. Moreover, interface-capturing schemes introduce several numerical

challenges, including mass and momentum dissipation at the interface Koch et al. (2016), smearing of fine surface structures Boniou et al. (2022), and inaccuracies in the interaction between acoustic waves and interfaces Schmidmayer et al. (2023).
The employed solver, ALPACA, meets these requirements, having been specifically developed to study compressible and multiphase phenomena Hoppe et al. (2022a). The solvers in ALPACA utilize high-order, non-dissipative numerical schemes to accurately capture shockwaves Hoppe et al. (2022b). The meshing process is highly efficient, leveraging a multiresolution algorithm proposed by Harten (1995) that automatically refines the mesh as needed. The ALPACA solver has been extensively applied to a wide range of multiphase flow problems involving bubble and droplet dynamics. Kaiser et al. (2020) employed ALPACA to investigate the fragmentation of a cylindrical liquid drop following shock passage and reported agreement with experiments. Hoppe et al. (2022b) demonstrated its capability by accurately reproducing various shock wave – bubble interactions. More recently, the solver has been used to study bubble jetting near solid boundaries Bußmann et al. (2023); Mur et al. (2025), acoustically driven bubble oscillations Nagy et al. (2025); Nagy and Hegedűs (2025), shock-induced bubble collapses Biller et al. (2022), and laser-induced bubble jets Fan et al. (2024); Bußmann et al. (2022).

2.2.1 Governing Equations

The governing equations of compressible fluid flow that are solved in ALPACA are given by

$$\frac{\partial \rho}{\partial t} = -\nabla \cdot \rho \boldsymbol{u}, \tag{5}$$

$$\frac{\partial \rho \boldsymbol{u}}{\partial t} = -\nabla \cdot \left(\rho \boldsymbol{u} \otimes \boldsymbol{u} - \Pi\right), \tag{6}$$

$$\frac{\partial \rho E}{\partial t} = -\nabla \cdot \left(\rho E \boldsymbol{u} - \Pi \boldsymbol{u}\right), \tag{7}$$

where ρ is the density, $\boldsymbol{u}$ is the velocity, E is the specific energy and Π is the stress tensor. The stress tensor is

$$\Pi = -p\boldsymbol{I} + \mu_1 \left(\nabla \otimes \boldsymbol{u} + (\nabla \otimes \boldsymbol{u})^{\mathrm{tr}} - \frac{2}{3}\boldsymbol{I}\nabla \cdot \boldsymbol{u}\right) + \mu_2 \boldsymbol{I}\nabla \cdot \boldsymbol{u}, \tag{8}$$

where p is the pressure, $\mu_1 = \mu_s$ is the shear viscosity, $\mu_2 = \mu_b - 2/3\mu_s$ where μ_b is the bulk viscosity and $\boldsymbol{I}$ is the identity matrix. This formulation neglects the effect of gravity, heat conduction and phase change. ALPACA solves the governing equations given in Eq. (5)-(7) on adaptive rectangular domains via finite volume methods. Convective fluxes are calculated via a Riemann Solver based on Roe (1981) and then reconstructed via a WENO5 scheme given in Fu et al. (2016).
Two different interface capturing schemes are used in this study: a sharp level set method Osher and Fedkiw (2001) providing high geometric accuracy but prone to mass dissipation, and a diffuse-interface method Paula et al. (2023) that perfectly fulfills the conservation laws at the expense of a smeared interface region.

2.2.2 Level Set Method

The level set method is based on the level set function $\phi(t, x, y, z)$, that denotes the signed non-dimensional distance from the interface. The evolution of this function is governed by the advection equation

$$\frac{\partial \phi}{\partial t} + \mathbf{u}_\phi \cdot \nabla \phi = 0, \tag{9}$$

where $\mathbf{u}_\phi$ is the interface velocity obtained from a linearized Riemann solver that includes surface tension Luo et al. (2015). The interface is implicitly defined by the zero isosurface of the level set, $\phi = 0$. Positive ϕ values correspond to the primary phase, and negative values to the secondary phase. As ϕ evolves, numerical errors lead to deviations from the signed-distance property. To restore this property, a reinitialization procedure is applied at each time step by solving

$$\frac{\partial \phi}{\partial \tau} = \mathrm{sgn}(\phi_0)\,(1 - |\nabla \phi|), \tag{10}$$

where ϕ_0 is the pre-reinitialized field and τ is the pseudo-time. This equation is discretized spatially then advanced in pseudo-time with an explicit Euler step until steady state is reached (Hoppe et al., 2022a). The resulting level set is further smoothed using a WENO3 reconstruction to ensure numerical stability. To prevent unphysical far-field fluctuations, a level set cutoff is imposed, in this study $|\phi| \leq 8$.
Although level set methods inherently suffer from minor mass loss at the interface due to reinitialization errors (Nourgaliev and Theofanous, 2007), this issue can be mitigated by monitoring the total bubble mass throughout the simulation. Despite this limitation, the approach offers some advantages for studying non-spherical bubble dynamics, including a sharper interface localization with minimal numerical diffusion. A ghost cell method is employed at the interface for extension required due to the high order numerical methods Osher et al. (2004). Observe that the level set method does not smear the interface and each point in space clearly assigned to one of the phases; thus, the governing equations are always solved for a single-phase.

2.2.3 Diffuse-Interface Method

The diffuse-interface method differs significantly from the level set. In that case, there is a diffuse zone between the phases where both phases are simultaneously present. The governing equations are modified with the volume fraction of each phase, then written

and solved for each phase separately as given in Saurel and Abgrall (1999). The modified equations are not presented here. The indicator field α_i that represents the volume fraction of the i^{th} phase is also governed by a conservation law as

$$\frac{\partial \alpha_i}{\partial t} + \mathbf{u}_{\text{int}} \cdot \nabla \alpha_i = 0, \tag{11}$$

where $\mathbf{u}_{\text{int}}$ is the interface velocity. The phases are further coupled by the admissibility condition, that is

$$\sum_i \alpha_i = 1, \quad 0 \leq \alpha_i \leq 1. \tag{12}$$

The diffuse-interface capturing is implemented within a discrete-equation model where the fluxes are found from Riemann problems Abgrall and Saurel (2003). Currently, ALPACA employs RDEMIC, introduced by Paula et al. (2023), that is an extension of the traditional discrete-equation model that enables high-order volume-fraction reconstruction while preserving the robustness and stability. It achieves this by introducing a carefully designed discretization of fluxes and exchange terms based on reconstructed volume fractions, leading to accurate and stable interface representation even in complex multiphase interactions. Furthermore, the effect of surface tension is included at the interface as a source term in the equations, and the required surface curvature is calculated following reconstruction. The interested reader is referred to the original publication in Paula et al. (2023) for more details and implementation of the diffuse-interface.

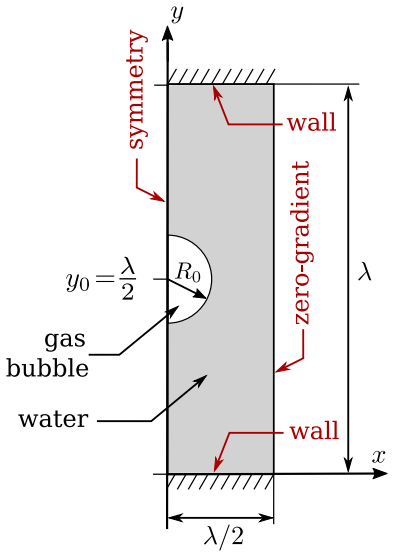

Fig. 1: Layout and boundary conditions of the axisymmetric DNS simulations.

2.2.4 Numerical setup

ALPACA is used to carry out two-dimensional axisymmetric numerical simulations of bubbles in a standing acoustic wave in water. The bubble was positioned at the node of the acoustic standing wave within a rectangular domain of dimensions $\lambda \times \lambda/2$, where λ is the wavelength. The boundary conditions are illustrated in Fig. 1. Reflective walls were placed on the south and north boundaries, causing wave reflections. A zero-gradient boundary condition was applied on the east boundary, while the west boundary served as the axis of symmetry. The standing wave in the water was introduced through the initial conditions as follows:

$$p(y) = p_0, \tag{13}$$

$$v(y) = -\frac{p_A}{c\rho_0} \sin(ky), \tag{14}$$

$$\rho(y) = \rho_0, \tag{15}$$

where $k = 2\pi/\lambda$ is the wave number, λ is the wavelength, p_0 is the ambient pressure, ρ_0 is the density of water at room temperature and c is the speed of sound. The bubble placed in the pressure antinode at $y = \lambda/2$ then experiences the following pressure:

$$p(t) = p_0 - p_A \cdot \sin(2\pi f \cdot t). \tag{16}$$

The derivation of the above equations can be found in Nagy et al. (2025). The initial conditions in the gas phase correspond to the equilibrium condition for a homogenous bubble, that is

$$p_{B,0} = p_0 + \frac{2\sigma}{R_0}, \tag{17}$$

where $p_{B,0}$ is the initial bubble pressure, σ is the surface tension and R_0 corresponds to the equilibrium radius. The initial velocities are zero and the density is set according to the ideal gas law:

$$\rho_{B,0} = \frac{p_{B,0}}{(\gamma_B - 1) c_V T_B}, \tag{18}$$

In both phases, the stiffened gas equation of state is used based on Harlow and Amsden (1971):

$$p = (\gamma - 1)\rho e - p_\infty, \tag{19}$$

where e is the internal energy and γ, p_∞ are parameters. In the gas phase $p_{\infty,B} = 0$, thus the stiffened gas EoS results in the ideal gas law, in which $\gamma_B = 1.4$ is the ratio of specific heats. To model the water, parameters $\gamma_L = 4.4$ and $p_{\infty,L} = 6 \cdot 10^8$ Pa are adopted from Kaiser et al. (2019).
To accelerate the formation of surface mode oscillations, the bubble shape is initially perturbed with relative mode amplitudes of $a_2/R = 0.031$, $a_3/R = -0.050$, $a_4/R = 0.008$, and $a_5/R = 0.016$. These amplitudes are chosen to ensure that the volume of the bubble remains unchanged. Each level set-based DNS simulation ran for 24 hours on the SUPERMUC-NG supercomputer, utilizing one compute node with 36 cores. The diffuse-interface-based DNS simulations run on the Komondor supercomputer on 32 cores of one compute node for 24 hours. In most cases, this computing time was sufficient to run the simulations for at least 10 acoustic cycles, enabling the analysis of long-term behavior.

2.3 Post-processing of DNS results

A post-processing code was developed in Paraview to extract the bubble radius and mode amplitudes from the numerical simulations. The radius of a non-spherical bubble cannot be defined uniquely; therefore, an equivalent bubble radius $\hat{R}(t)$ is introduced based on the instantaneous bubble volume $V_b(t)$ as

$$\frac{4}{3}\pi \hat{R}^3(t) = V_b(t), \tag{20}$$

where $V_b(t)$ is obtained by integrating over all computational cells located inside the bubble. A cell with index i is considered to be inside the bubble if $\phi_i < 0$, where ϕ_i denotes the level set value of that cell. Accordingly, the set of internal cells can be expressed as $C_b(t) = \{i \mid \phi_i(t) < 0\}$. For two-dimensional axisymmetric simulations with axial coordinate y and radial coordinate x, the bubble volume is evaluated by revolving each cell volume element around the symmetry axis:

$$V_b(t) = \sum_{i \in C_b(t)} V_i = 2\pi \sum_{i \in C_b(t)} x_i \, a_i^2, \tag{21}$$

where x_i is the radial position of the i^{th} cell and a_i is its edge length. For comparison with the reduced-order model, it is also necessary to quantify the amplitude of surface oscillations. The instantaneous bubble contour is represented as a generalized Fourier series,

$$r(\theta, t) = \sum_{n=0}^{\infty} a_n(t) P_n(\cos\theta), \tag{22}$$

where P_n denotes the Legendre polynomial of order n, and $a_n(t)$ represents the mode amplitude. The Fourier coefficients in a single time step are evaluated according to

$$a_n = \frac{2n+1}{2} \int_0^\pi P_n(\cos\theta)\, r(\theta)\, \sin\theta \, d\theta. \tag{23}$$

The numerical evaluation of Eq. (23) from discrete simulation data proceeds as follows. At each time step, cells located near the bubble interface are first identified based on the criterion $|\phi_i(t)| < \varepsilon_s$, where $\varepsilon_s = 0.6$ is the selection threshold. This yields the set $C_{\text{int}}(t)$ containing the interface cells. The Cartesian coordinates (x_i, y_i) of these cells are then transformed to polar coordinates relative to the bubble center (x_0, y_0) according to

$$r_i = \sqrt{(x_i - x_0)^2 + (y_i - y_0)^2}, \quad \theta_i = \arctan\left(\frac{x_i - x_0}{y_i - y_0}\right), \tag{24}$$

and subsequently ordered by increasing θ_i. The discrete approximation of Eq. (23) is computed as

$$a_n = \frac{2n+1}{2} \frac{1}{N_{\text{int}}} \sum_{j=1}^{N_{\text{int}}} P_n(\cos\theta_j)\, r_j \, \sin\theta_j \, (\theta_j - \theta_{j-1}), \tag{25}$$

where N_{int} denotes the number of interface points, and (θ_j, r_j) represents the ordered set of polar coordinates. The calculation was then repeated for each time step, and the mode amplitudes were obtained as a function of time.

3 Results

This section presents the results of the ALPACA and ROM simulations. ALPACA simulations are conducted using both the level set (LS) and diffuse-interface (DI) methods, as referenced throughout this section. First, the convergence of the ALPACA simulations is analyzed by increasing the mesh resolution and comparing the results to ROM predictions. Then, the effect of the pressure amplitude is explored for a selected case.

3.1 Mesh independence study

A bubble with an initial radius of $R_0 = 10.5\,\mu\text{m}$ is excited by a standing wave with an amplitude of $p_A = 50\,\text{kPa}$ and a frequency of $f = 480\,\text{kHz}$. This case is selected because, according to the ROM, a stable 3$^{\text{rd}}$-mode oscillation is expected to form with a relatively large amplitude, that DNS simulations should be able to handle properly.

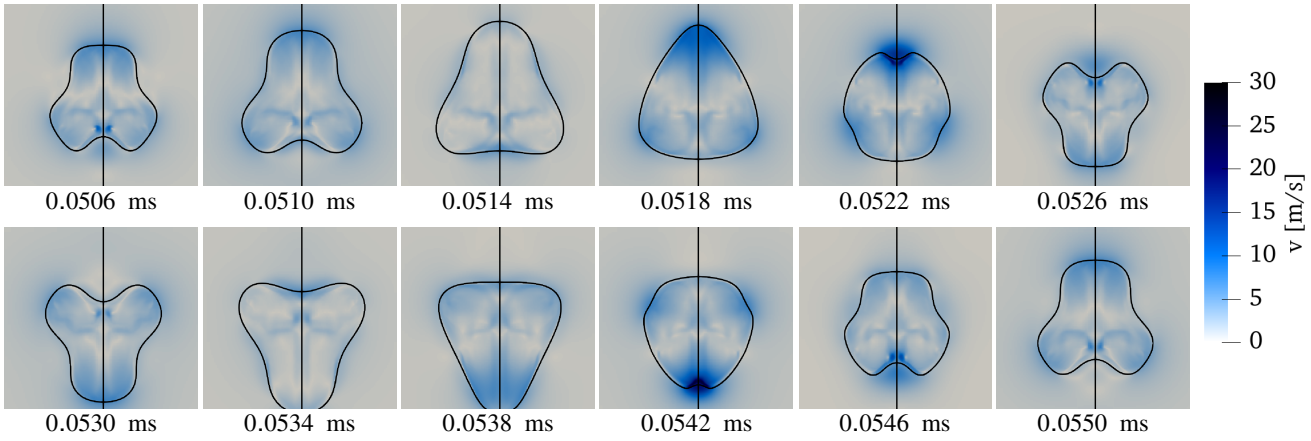

Fig. 2: Snapshots of the stable surface mode oscillation forming in the DI-based simulation with parameters $R_0 = 10.5\,\mu\text{m}$, $p_A = 50\,\text{kPa}$ and $f = 480\,\text{kHz}$.

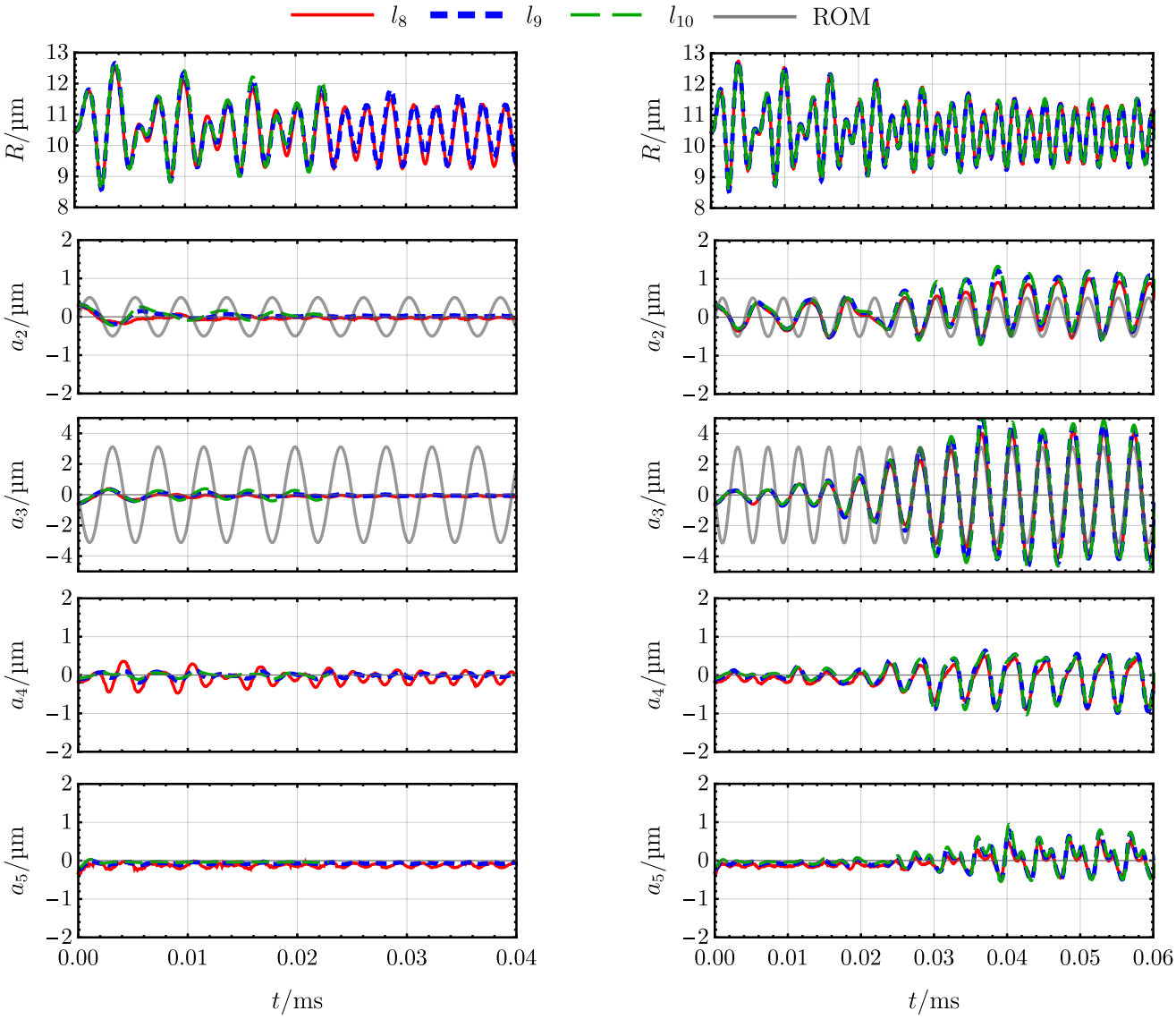

(a) DNS with level set (b) DNS with diffuse interface

Fig. 3: Results of the convergence study with parameters $R_0 = 10.5\,\mu\text{m}$, $p_A = 50\,\text{kPa}$ and $f = 480\,\text{kHz}$. The test interface capturing methods are the level set in column (a) and the diffuse-interface in column (b).

Simulations were conducted in ALPACA using three different mesh resolutions. The number of adaptive refinements was varied from 8 to 10 on an initial 80×144 mesh, resulting in the number of cells along the bubble diameter being $N_{\text{bubble}} = 76$, 152, and 304 for the resolutions l_8, l_9 and l_{10}, respectively. Following an initial perturbation and approximately 15 acoustic cycles, a stable surface-mode oscillation develops. The resulting bubble shapes are shown in Fig. 2. Notably, only the DI method captures this stable surface-mode oscillation, whereas in the LS simulations, the initial perturbation decays even at the highest resolution. The stable third mode oscillation has a period of approximately 0.004 ms, that is twice the period of the acoustic excitation (0.002 ms).

Figure 3 quantitatively depicts the bubble radius and mode amplitudes obtained using both interface-capturing methods. The top row shows the bubble radius, which is quite insensitive to mesh resolution, indicating that even the low resolution (l_8) is sufficient to capture the spherical dynamics. The second and third rows of Fig. 3 show the amplitudes of the second and third surface modes, respectively. The gray line represents the surface mode amplitudes predicted by the ROM after a long transient (i.e., the transient is omitted).

It is evident that the LS method artificially damps the surface mode amplitudes, whereas the DI method accurately reproduces the ROM predictions following the initial transient. Convergence is achieved at medium resolution (l_9) for both LS and DI, as further refinement does not significantly alter the dynamics. The amplitudes of the higher modes remain small, with $a_3 = 0.24\,\mu\text{m}$ and $a_4 = 0.15\,\mu\text{m}$ according to the ROM, and similarly limited in both LS and DI results.

Based on these observations, a mesh resolution of $N_{\text{bubble}} \geq 150$ (l_9 or higher) is sufficient to accurately capture both the radial dynamics and surface mode amplitudes. All subsequent simulations are conducted using $N_{\text{bubble}} \geq 150$ to ensure accuracy. These results also demonstrate that the DI method is required for accurately capturing surface mode oscillations, while the LS method artificially damps these modes; at least in the above presented case.

3.2 Effect of pressure amplitude

The effect of increasing pressure amplitude is examined for a bubble with an initial radius of $R_0 = 47.5\,\mu\text{m}$, excited by an acoustic standing wave of frequency $f = 30\,\text{kHz}$ at various pressure amplitudes using ALPACA. According to the ROM predictions, this case is particularly interesting: the bubble remains spherical when the driving pressure amplitude p_A is below 19 kPa. For amplitudes exceeding 39 kPa, unstable surface-mode oscillations occur ($a_n \to \infty$), potentially leading to bubble breakup. In the intermediate range, $19\,\text{kPa} < p_A < 39\,\text{kPa}$, stable 2^{nd}- and 3^{rd}-mode oscillations are expected to develop.

Direct numerical simulations were performed for three representative pressure amplitudes. Figure 4a–c shows snapshots from the DI-based simulations at $p_A = 10\,\text{kPa}$, 32 kPa, and 42 kPa, respectively. For the 10 kPa case, the initial non-spherical perturbation decays, resulting in a nearly spherical bubble at $t = 0.3$ ms, as shown in Fig. 4a. At $p_A = 32\,\text{kPa}$, a pronounced transient 3^{rd}-mode oscillation develops as shown in Fig. 4b, after which only a weak residual surface mode remains. At the highest investigated pressure amplitude, $p_A = 42\,\text{kPa}$ in Fig. 4c, the surface-mode instability grows rapidly, leading to bubble breakup at $t = 0.063$ ms in the DI simulation.

The radius–time curves are shown at the top of Fig. 4d–f. The radial dynamics exhibit remarkable quantitative agreement between the ALPACA simulations using both interface models (red line: level set; dashed blue line: diffuse-interface) and the ROM predictions (black line). For example, at $p_A = 10\,\text{kPa}$ and 32 kPa, the agreement is excellent during the first 12 oscillation periods. For the high pressure amplitude case in Fig. 4f, the dots indicate the time of bubble breakup for the different models. Although minor discrepancies arise in the bubble radius near breakup, the predicted breakup times agree closely among the models, with breakup consistently occurring after the second collapse of the bubble.

The corresponding mode amplitude–time curves are presented in the lower panels of Fig. 4d–f, showing some trends between DNS and ROM simulations. At the lowest pressure amplitude ($p_A = 10\,\text{kPa}$), the initial perturbations in the surface modes decay rapidly, indicating spherical stability of the bubble under these parameters. The damping behavior is nearly identical in the ROM and DI simulations, while the LS model predicts a slightly faster decay of the surface modes. At an intermediate pressure amplitude ($p_A = 32\,\text{kPa}$), a strong transient 3^{rd}-mode oscillation appears during the first few acoustic cycles in all models, with excellent agreement between the DI and ROM results. After the transient, a combination of stable 2^{nd}- and 3^{rd}-mode oscillations persists in the ROM, while the DI-based DNS shows similar behavior with a weak additional 4^{th}-mode contribution. In contrast, the LS-based simulations exhibit complete damping of the 3^{rd} and 4^{th} modes, leaving only a small residual 2^{nd}-mode oscillation.

At the highest pressure amplitude ($p_A = 42\,\text{kPa}$), the initial perturbations grow rapidly, leading to bubble breakup at $t = 0.072$ ms in the LS simulation and at $t = 0.063$ ms in the DI simulation, as indicated by the markers in Fig. 4f. For this parameter set, the ROM predicts diverging mode amplitudes ($a_n \to \infty$) and fails at $t = 0.061$ ms. Up to the point of breakup, the mode amplitudes remain in close agreement among the models, demonstrating that all approaches can capture the growth of large-amplitude surface modes leading to instability and bubble break-up.

4 Discussion

First, the convergence of the DNS simulations was verified in Section 3.1. The ALPACA simulations achieved convergence with a bubble resolution of approximately $N_{\text{bubble}} = 150$, meaning that the bubble diameter had to be resolved with at least 150 cells. Further resolving the bubble did not change the results meaningfully. However, numerical convergence does not imply physical accuracy, since simulations using different interface-capturing methods converge toward different solutions as the resolution is increased. Based on the results, we consider the DI-based DNS to be more physically accurate, as it agrees closely with the ROM predictions, which have been validated against experiments in Kalmár et al. (2024).

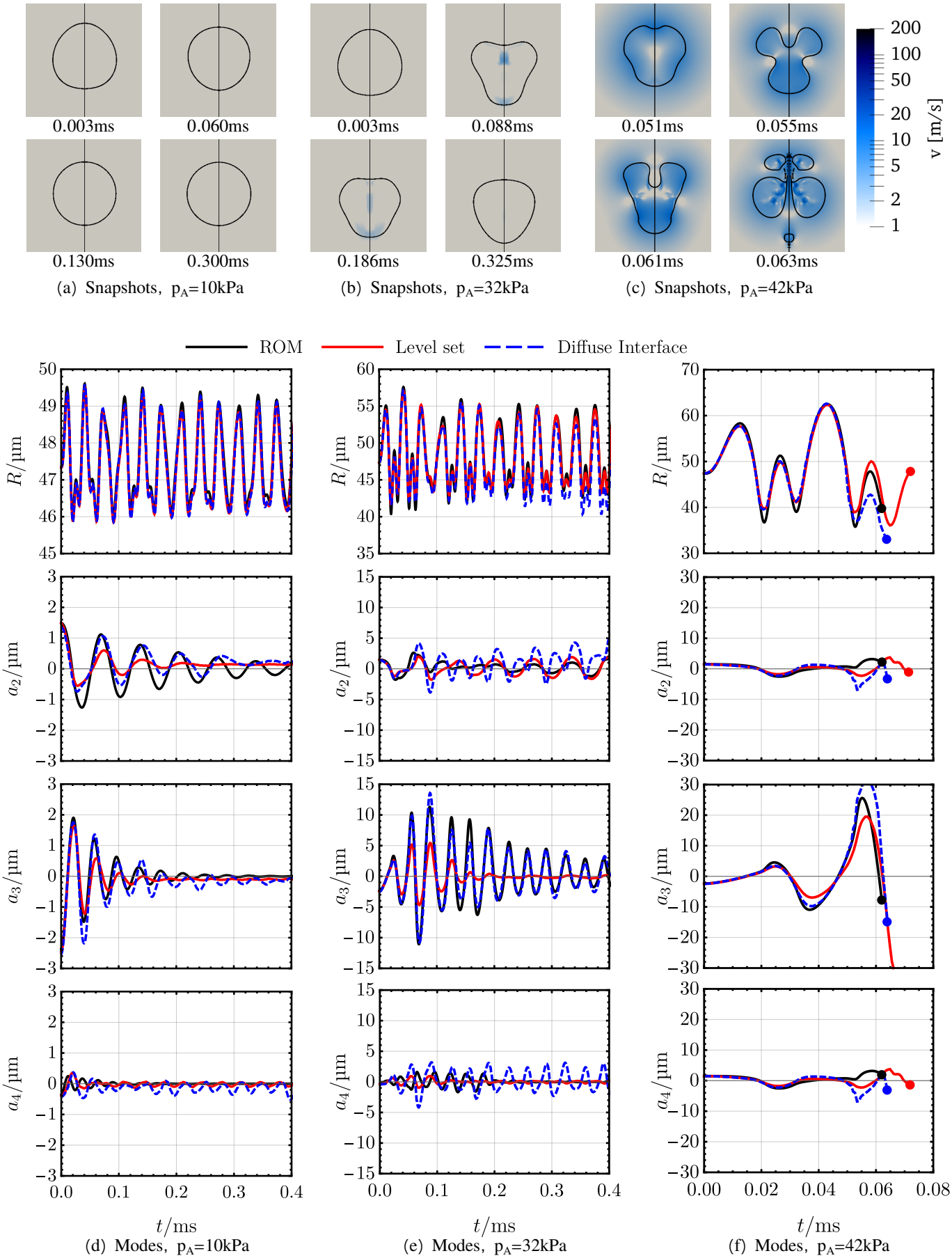

(a) Snapshots, p_A=10kPa (b) Snapshots, p_A=32kPa (c) Snapshots, p_A=42kPa

(d) Modes, p_A=10kPa (e) Modes, p_A=32kPa (f) Modes, p_A=42kPa

Fig. 4: Summary of results for a $R_0 = 47.5\,\mu$m bubble excited with $f = 30\,$kHz and various pressure amplitude ultrasound. Panels (a)-(c) depict snapshots of the velocity magnitude (see legend) and bubble interface (black contour) from the DI-based DNS simulations. Panels (d)-(f) show the mode amplitudes as a function of time with the 3 different approaches: ROM (black line), LS-based DNS (red line) and DI-based DNS (dashed blue line).

Two distinct physical mechanisms can be identified in the investigated cases. The radial oscillation of the bubble primarily depends on accurately capturing the forces associated with liquid inertia, whereas the small-amplitude surface mode oscillations are strongly influenced by capillary forces (i.e., surface tension). The radial dynamics – given as the function $R(t)$ – are computed from the bubble volume in the DNS and from the Keller–Miksis equation in the ROM. These show excellent agreement for both interface-capturing methods, even at relatively low mesh resolutions. Because the radial oscillations are dominated by inertial effects and capillary forces are less significant, both the DI and LS methods provide accurate predictions for the spherical component of the motion.

The comparison of mode dynamics further confirms that the DI-based DNS simulations and the ROM predict similar behavior. For bubbles that are expected to be spherically stable under the given excitation, perturbations in the mode amplitudes decay similarly in both models. For bubbles that are close to instability but do not yet break up, the agreement in mode curves remains strong. The onset of bubble breakup is also captured similarly. In contrast, the LS-based DNS systematically overdamps the mode amplitudes, leading to non-physical suppression of surface oscillations that was observed before in Nagy et al. (2025). This discrepancy likely originates from differences in how capillary forces are treated at the interface. A sharper and more localized representation of the interface has recently been shown to improve curvature evaluation and reduce parasitic currents and numerical damping Gorges et al. (2025); such methods in the future could also be used to study non-spherical bubble oscillations more accurately.

One of the most interesting findings concerns the prediction of bubble breakup. In theory, the ROM is based on a small-perturbation assumption, whereas the DNS simulations should be accurate for large-amplitude deformations as well. Bubble breakup is associated with the divergence of mode amplitudes, at which point the validity of the ROM becomes questionable. Nevertheless, the ROM still successfully identifies the onset of instability, as the predicted breakup times are remarkably similar between the ROM and DNS models. Furthermore, the LS-based DNS simulations could also reproduce the bubble break-up after the second bubble collapse.

These results suggest that the ROM can serve as a computationally efficient tool to identify the parameter ranges where bubbles can break up, while DNS simulations provide detailed flow-field information and accurately capture the evolution of high-amplitude surface modes near bubble breakup. Together, the two approaches offer complementary insights: ROM can be used to efficiently map the regions of instability in parameter space, and DI-based DNS simulations can subsequently verify and analyze selected cases in greater physical detail.

5 Conclusion

In conclusion, both the ROM and DMS simulations with the diffuse-interface predict similar non-spherical bubble oscillations, confirming their reliability to qualitatively describe complex bubble dynamics. The diffuse-interface–based DNS results show excellent quantitative agreement with the ROM predictions, particularly in cases where the bubble remains spherically stable or exhibits moderate surface-mode oscillations, while the level set formulation–although accurate for inertia-driven radial oscillations–tends to overdamp surface modes. The results further demonstrate that diverging mode amplitudes in the ROM effectively indicate the onset of bubble breakup, even beyond the formal small-amplitude validity of the model. This suggests that ROM provides a computationally efficient tool for identifying breakup limits in parameter space, whereas DNS simulations with the diffuse-interface model can capture the process in more physical detail.

Acknowledgements

Project No. 2025-2.1.2-EKÖP-KDP-2025-00005 has been implemented with the support provided by the Ministry of Culture and Innovation of Hungary, from the National Research, Development and Innovation Fund, financed under the EKÖP_KDP-25-1-BME-6 funding scheme. The authors gratefully acknowledge the Gauss Centre for Supercomputing e.V. (www.gauss-centre.eu) for funding this project by providing computing time on the GCS Supercomputer SuperMUC-NG at Leibniz Supercomputing Centre (www.lrz.de). We acknowledge the Digital Government Development and Project Management Ltd. for awarding us access to the Komondor HPC facility based in Hungary. Project no. TKP-6-6/PALY-2021 has been implemented with the support provided by the Ministry of Culture and Innovation of Hungary from the National Research, Development and Innovation Fund, financed under the TKP2021-NVA funding scheme. The authors acknowledge the financial support of the Hungarian National Research Development and Innovation Office via NKFIH grants OTKA FK142376 and OTKA PD142254.

References

Rémi Abgrall and Richard Saurel. Discrete equations for physical and numerical compressible multiphase mixtures. *Journal of Computational Physics*, 186(2):361–396, 2003. doi: 10.1016/S0021-9991(03)00011-1.

Ahmad Al-Awamleh and Ferenc Hegedűs. Sono-hydrogen: a theoretical investigation of its energy intensity. *Periodica Polytechnica Mechanical Engineering*, 68(3):254–263, 2024. doi: 10.3311/PPme.37299.

Benedikt Biller, Nils Hoppe, Stefan Adami, and Nikolaus A Adams. Jetting mechanisms in bubble-pair interactions. *Physics of Fluids*, 34(7), 2022. doi: 10.1063/5.0097039.

Victor Boniou, Thomas Schmitt, and Aymeric Vié. Comparison of interface capturing methods for the simulation of two-phase flow in a unified low-mach framework. *International Journal of Multiphase Flow*, 149:103957, 2022. doi: 10.1016/j.ijmultiphaseflow.2021.103957.

Alexander Bußmann, Stefan Adami, and Nikolaus A Adams. A systematic calibration procedure for bubble dynamics for laser ablation in liquids. *Nanobubble Production 7*, page 72, 2022.

Alexander Bußmann, Farbod Riahi, Bilal Gökce, Stefan Adami, Stephan Barcikowski, and Nikolaus A Adams. Investigation of cavitation bubble dynamics near a solid wall by high-resolution numerical simulation. *Physics of Fluids*, 35(1), 2023. doi: 10.1063/5.0135924.

Sangyeon Cho and Seok Hyun Yun. Structure and optical properties of perovskite-embedded dual-phase microcrystals synthesized by sonochemistry. *Communications Chemistry*, 3(1):1–7, 2020. doi: 10.1038/s42004-020-0265-6.

Sarah Cleve, M Guédra, Cyril Mauger, C Inserra, and P Blanc-Benon. Microstreaming induced by acoustically trapped, non-spherically oscillating microbubbles. *Journal of Fluid Mechanics*, 875:597–621, 2019. doi: 10.1017/jfm.2019.511.

Fabian Denner, Fabien Evrard, and Berend Van Wachem. Modeling acoustic cavitation using a pressure-based algorithm for polytropic fluids. *Fluids*, 5(2):69, 2020. doi: 10.3390/fluids5020069.

Yuzhe Fan, Alexander Bußmann, Fabian Reuter, Hengzhu Bao, Stefan Adami, José M Gordillo, Nikolaus Adams, and Claus-Dieter Ohl. Amplification of supersonic microjets by resonant inertial cavitation-bubble pair. *Physical Review Letters*, 132(10):104004, 2024. doi: 10.1103/PhysRevLett.132.104004.

Lin Fu, Xiangyu Y Hu, and Nikolaus A Adams. A family of high-order targeted eno schemes for compressible-fluid simulations. *Journal of Computational Physics*, 305:333–359, 2016. doi: 10.1016/j.jcp.2015.10.037.

Christian Gorges, Fabien Evrard, Robert Chiodi, Berend van Wachem, and Fabian Denner. Sharp front tracking with geometric interface reconstruction. *Journal of Computational Physics*, 535:114059, 2025. doi: 10.1016/j.jcp.2025.114059.

Matthieu Guédra and Claude Inserra. Bubble shape oscillations of finite amplitude. *Journal of Fluid Mechanics*, 857:681–703, 2018. doi: 10.1017/jfm.2018.768.

Francis H Harlow and Anthony A Amsden. Fluid dynamics. a lasl monograph. Technical report, Los Alamos National Lab.(LANL), Los Alamos, NM (United States), 1971.

Ami Harten. Multiresolution algorithms for the numerical solution of hyperbolic conservation laws. *Communications on Pure and Applied Mathematics*, 48(12):1305–1342, 1995. doi: 10.1002/cpa.3160481201.

Nils Hoppe, Stefan Adami, and Nikolaus A. Adams. A parallel modular computing environment for three-dimensional multiresolution simulations of compressible flows. *Computer Methods in Applied Mechanics and Engineering*, 391:114486, 2022a. doi: 10.1016/j.cma.2021.114486.

Nils Hoppe, Josef M. Winter, Stefan Adami, and Nikolaus A. Adams. Alpaca - a level-set based sharp-interface multiresolution solver for conservation laws. *Computer Physics Communications*, 272:108246, 2022b. doi: 10.1016/j.cpc.2021.108246.

Xuelan Hou, Changsheng Chen, Lincan Fang, Jiasi Li, Yihao Huang, Ye Zhu, James Kwan, and Shik Chi Edman Tsang. Catalytic ammonia decomposition using single high-frequency ultrasound. *The Journal of Physical Chemistry C*, 129(35):15571–15577, 2025. doi: 10.1021/acs.jpcc.5c05410.

Boxin Jia and Hitoshi Soyama. Non-spherical cavitation bubbles: A review. *Fluids*, 9(11):249, 2024. doi: 10.3390/fluids9110249.

Jakob WJ Kaiser, Nils Hoppe, Stefan Adami, and Nikolaus A Adams. An adaptive local time-stepping scheme for multiresolution simulations of hyperbolic conservation laws. *Journal of Computational Physics*, 4:100038, 2019. doi: 10.1016/j.jcpx.2019.100038.

Jakob WJ Kaiser, Josef Winter, Stephan Adami, and Nikolaus A Adams. Investigation of interface deformation dynamics during high-weber number cylindrical droplet breakup. *International Journal of Multiphase Flow*, 132:103409, 2020. doi: 10.1016/j.ijmultiphaseflow.2020.103409.

Péter Kalmár, Ferenc Hegedűs, Dániel Nagy, Levente Sándor, and Kálmán Klapcsik. Memory-friendly fixed-point iteration method for nonlinear surface mode oscillations of acoustically driven bubbles: from the perspective of high-performance gpu programming. *Ultrasonics Sonochemistry*, 99:106546, 2023. doi: 10.1016/j.ultsonch.2023.106546.

Péter Kalmár, Ferenc Hegedűs, and Kálmán Klapcsik. A comparative study of measurements and numerical simulations of acoustically excited non-spherical bubbles oscillation. *International Journal of Multiphase Flow*, 179:104947, 2024. doi: 10.1016/j.ijmultiphaseflow.2024.104947.

Masaharu Kameda and Yoichiro Matsumoto. Nonlinear oscillation of a spherical gas bubble in acoustic fields. *The Journal of the Acoustical Society of America*, 106(6):3156–3166, 1999. doi: 10.1121/1.428170.

Max Koch, Christiane Lechner, Fabian Reuter, Karsten Köhler, Robert Mettin, and Werner Lauterborn. Numerical modeling of laser generated cavitation bubbles with the finite volume and volume of fluid method, using openfoam. *Computers & Fluids*, 126:71–90, 2016. doi: 10.1016/j.compfluid.2015.11.008.

Ferenc Kubicsek, Áron Kozák, Tamás Turányi, István Gyula Zsély, Máté Papp, Ahmad Al-Awamleh, and Ferenc Hegedûs. Ammonia production by microbubbles: A theoretical analysis of achievable energy intensity. *Ultrasonics Sonochemistry*, 106: 106876, 2024. doi: 10.1016/j.ultsonch.2024.106876.

Ferenc Kubicsek, Ferenc Hegedűs, and Péter Csizmadia. Optimization of sonochemical ammonia synthesis in non-newtonian fluids. *Archive of Mechanical Engineering*, pages 379–403, 2025. doi: 10.24425/ame.2025.154740.

Jian Luo, XY Hu, and Nikolaus A Adams. A conservative sharp interface method for incompressible multiphase flows. *Journal of Computational Physics*, 284:547–565, 2015. doi: 10.1016/j.jcp.2014.12.044.

Yan Ma, Guoqian Zhang, and Tao Ma. Interaction of two bubbles with distortion in an acoustic field. *Ultrasonics Sonochemistry*, 84:105953, 2022. doi: 10.1016/j.ultsonch.2022.105953.

Dominik Mnich, Fabian Reuter, Fabian Denner, and Claus-Dieter Ohl. Single cavitation bubble dynamics in a stagnation flow. *Journal of Fluid Mechanics*, 979:A18, 2024. doi: 10.1017/jfm.2023.1048.

Jaka Mur, Fabian Reuter, Vid Agrež, Claus-Dieter Ohl, et al. Optic generation and perpetuation of acoustic bubble clusters. *Ultrasonics Sonochemistry*, 110:107023, 2024. doi: 10.1016/j.ultsonch.2024.107023.

Jaka Mur, Alexander Bußmann, Thomas Paula, Stefan Adami, Nikolaus A Adams, Claus-Dieter Ohl, et al. Micro-jet formation induced by the interaction of a spherical and toroidal cavitation bubble. *Ultrasonics Sonochemistry*, 112:107185, 2025. doi: 10.1016/j.ultsonch.2024.107185.

Dániel Nagy and Ferenc Hegedűs. Az alpaca szoftver validációja akusztikusan gerjesztett gázbuborékok szimulációjára: Validation of alpaca for the simulation of acoustically excited gas bubbles. *Nemzetközi Gépészeti Konferencia–OGÉT*, pages 360–365, 2023.

Dániel Nagy and Ferenc Hegedűs. Suppressing the jet formation in a bubble pair excited with an ultrasonic pulse. *Ultrasonics Sonochemistry*, page 107349, 2025. doi: 10.1016/j.ultsonch.2025.107349.

Dániel Nagy, Stefan Adami, and Ferenc Hegedűs. Direct numerical simulation of spherical and non-spherical bubble dynamics using the alpaca compressible multiphase flow solver. *International Journal of Multiphase Flow*, page 105287, 2025. doi: 10.1016/j.ijmultiphaseflow.2025.105287.

Robert R Nourgaliev and Theo G Theofanous. High-fidelity interface tracking in compressible flows: unlimited anchored adaptive level set. *Journal of Computational Physics*, 224(2):836–866, 2007. doi: 10.1016/j.jcp.2006.10.031.

Stanley Osher and Ronald P Fedkiw. Level set methods: an overview and some recent results. *Journal of Computational physics*, 169(2):463–502, 2001. doi: 10.1006/jcph.2000.6636.

Stanley Osher, Ronald Fedkiw, and Krzysztof Piechor. Level set methods and dynamic implicit surfaces. *Applied Mechanics Reviews*, 57(3):B15–B15, 2004. doi: 10.1115/1.1760521.

Thomas Paula, Stefan Adami, and Nikolaus A. Adams. A robust high-resolution discrete-equations method for compressible multi-phase flow with accurate interface capturing. *Journal of Computational Physics*, 491:112371, 2023. doi: 10.1016/j.jcp.2023.112371.

Firdaus Prabowo and Claus-Dieter Ohl. Surface oscillation and jetting from surface attached acoustic driven bubbles. *Ultrasonics Sonochemistry*, 18(1):431–435, 2011. doi: 10.1016/j.ultsonch.2010.07.013.

Andrea Prosperetti and Y Hao. Modelling of spherical gas bubble oscillations and sonoluminescence. *Philosophical Transactions of the Royal Society of London. Series A: Mathematical, Physical and Engineering Sciences*, 357(1751):203–223, 1999. doi: 10.1098/rsta.1999.0324.

Philip L Roe. Approximate riemann solvers, parameter vectors, and difference schemes. *Journal of Computational Physics*, 43(2): 357–372, 1981. doi: 10.1016/0021-9991(81)90128-5.

JM Rosselló, W Lauterborn, M Koch, T Wilken, T Kurz, and R Mettin. Acoustically induced bubble jets. *Physics of Fluids*, 30 (12), 2018. doi: 10.1063/1.5063011.

Richard Saurel and Rémi Abgrall. A multiphase godunov method for compressible multifluid and multiphase flows. *Journal of Computational Physics*, 150(2):425–467, 1999. doi: 10.1006/jcph.1999.6187.

Kevin Schmidmayer, Joris Cazé, Fabien Petitpas, Eric Daniel, and Nicolas Favrie. Modelling interactions between waves and diffused interfaces. *International Journal for Numerical Methods in Fluids*, 95(2):215–241, 2023. doi: 10.1002/fld.5142.

Stephen J Shaw. Translation and oscillation of a bubble under axisymmetric deformation. *Physics of Fluids*, 18(7):072104, 2006. doi: 10.1063/1.2227047.

Stephen J Shaw. The stability of a bubble in a weakly viscous liquid subject to an acoustic traveling wave. *Physics of Fluids*, 21(2): 022104, 2009. doi: 10.1063/1.3076932.

Stephen J Shaw. Nonspherical sub-millimeter gas bubble oscillations: Parametric forcing and nonlinear shape mode coupling. *Physics of Fluids*, 29(12):122103, 2017. doi: 10.1063/1.5005599.

S Sochard, AM Wilhelm, and H Delmas. Modelling of free radicals production in a collapsing gas-vapour bubble. *Ultrasonics Sonochemistry*, 4(2):77–84, 1997. doi: 10.1016/S1350-4177(97)00021-7.

Michel Versluis, David E Goertz, Peggy Palanchon, Ivo L Heitman, Sander M van der Meer, Benjamin Dollet, Nico de Jong, and Detlef Lohse. Microbubble shape oscillations excited through ultrasonic parametric driving. *Physical review E*, 82(2):026321, 2010. doi: 10.1103/PhysRevE.82.026321.

Cherie CY Wong, Davide Bernardo Preso, Yi Qin, Pankaj S Sinhmar, Zhiyuan Zong, and James Kwan. Ultrasound-driven seawater splitting catalysed by tio2 for hydrogen production. *International Journal of Hydrogen Energy*, 111:723–734, 2025. doi: 10.1016/j.ijhydene.2025.02.327.

Yaorong Wu, Zhaokang Lei, Rui Liu, and Chenghui Wang. The oscillations of non-spherical bubbles in liquid. *Ultrasonics Sonochemistry*, 114:107262, 2025. doi: 10.1016/j.ultsonch.2025.107262.